



## Article

# High Curie Temperature Achieved in the Ferromagnetic $Mn_xGe_{1-x}/Si$ Quantum Dots Grown by Ion Beam Co-Sputtering

Xiaoxiao Duan <sup>1,†</sup> , Shuming Ye <sup>1,†</sup>, Jing Yang <sup>2</sup>, Chen Li <sup>1</sup>, Chunjiang Lu <sup>1</sup>, Xinpeng He <sup>1</sup>, Luran Zhang <sup>1</sup>, Rongfei Wang <sup>1,\*</sup>, Feng Qiu <sup>1</sup>, Jie Yang <sup>1,\*</sup>, Haoyang Cui <sup>3</sup> and Chong Wang <sup>1,\*</sup>

- <sup>1</sup> National Center for International Research on Photoelectric and Energy Materials, School of Materials and Energy, Yunnan University, Kunming 650091, China; duanxiaoxiao10@163.com (X.D.); ysming97@163.com (S.Y.); li18281543317@163.com (C.L.); chunjiangtenet@163.com (C.L.); valvrave@126.com (X.H.); zhangluran@ynu.edu.cn (L.Z.); fengqiu@ynu.edu.cn (F.Q.)
- <sup>2</sup> Key Lab of Polar Materials and Devices, Ministry of Education, East China Normal University, Shanghai 200241, China; jyang@ee.ecnu.edu.cn
- <sup>3</sup> College of Electronic and Information Engineering, Shanghai University of Electric Power, Shanghai 200090, China; cuihy@shiep.edu.cn
- \* Correspondence: rfwang@ynu.edu.cn (R.W.); jieyang@ynu.edu.cn (J.Y.); cwang@ynu.edu.cn (C.W.)
- † These authors contributed equally to this work.



**Citation:** Duan, X.; Ye, S.; Yang, J.; Li, C.; Lu, C.; He, X.; Zhang, L.; Wang, R.; Qiu, F.; Yang, J.; et al. High Curie Temperature Achieved in the Ferromagnetic  $Mn_xGe_{1-x}/Si$  Quantum Dots Grown by Ion Beam Co-Sputtering. *Nanomaterials* **2022**, *12*, 716. <https://doi.org/10.3390/nano12040716>

Academic Editor: Julián María González Estévez

Received: 7 January 2022

Accepted: 19 February 2022

Published: 21 February 2022

**Publisher's Note:** MDPI stays neutral with regard to jurisdictional claims in published maps and institutional affiliations.



**Copyright:** © 2022 by the authors. Licensee MDPI, Basel, Switzerland. This article is an open access article distributed under the terms and conditions of the Creative Commons Attribution (CC BY) license (<https://creativecommons.org/licenses/by/4.0/>).

**Abstract:** Ferromagnetic semiconductors (FMSs) exhibit great potential in spintronic applications. It is believed that a revolution of microelectronic techniques can take off, once the challenges of FMSs in both the room-temperature stability of the ferromagnetic phase and the compatibility with Si-based technology are overcome. In this article, the  $Mn_xGe_{1-x}/Si$  quantum dots (QDs) with the Curie temperature ( $T_C$ ) higher than the room temperature were grown by ion beam co-sputtering (IBCS). With the Mn doping level increasing, the ripening growth of MnGe QDs occurs due to self-assembly via the Stranski–Krastanov (SK) growth mode. The surface-enhanced Raman scattering effect of Mn sites observed in MnGe QDs are used to reveal the distribution behavior of Mn atoms in QDs and the Si buffer layer. The Curie temperature of  $Mn_xGe_{1-x}$  QDs increases, then slightly decreases with increasing the Mn doping level, and reaches its maximum value of 321 K at the doping level of 0.068. After a low-temperature and short-time annealing, the  $T_C$  value of  $Mn_{0.068}Ge_{0.932}$  QDs increases from 321 K to 383 K. The higher Ge composition and residual strain in the IBCS grown  $Mn_xGe_{1-x}$  QDs are proposed to be responsible for maintaining the ferromagnetic phase above room temperature.

**Keywords:** MnGe quantum dots; ferromagnetic nanostructure; Curie temperature; doping level

## 1. Introduction

In the last two decades, massive efforts have been devoted to probing one kind of multifunctional material, on which the so-called three golden disciplines, namely, optics, microelectronics, and magnetism, can be integrated organically, so that the optical, electronic, and magnetic responses can be modulated effectively in one kind of material by the external fields [1,2]. If it actualizes a new information technology, the spin electron substitutes for the charge as the information carrier, characterized by ultrafast transportation, high-capacity, ultra-wideband, and ultralow-power dissipation [1,3,4]. In that case, it is worthy of expecting such results in these kinds of materials. This technology can overcome many predicaments of the traditional charge electronics, since the interaction energy between spins is 1000 times less than that between charged electrons. In other words, changing the former states is much easier than that of the latter [5]. Diluted ferromagnetic semiconductors (DFMS) have been regarded as one of the most promising candidate materials for fulfilling this excellent integration engineering. Compared to the II-VI, III-V compounds, and halide perovskite counterparts [6], group-IV DFMSs have

continued to attract more attention due to their natural advantages of direct compatibility with Si-based microelectronic techniques and the higher Curie temperature ( $T_C$ ) observed in the previous work [4,7].

A  $T_C$  value much higher than room temperature ( $T_C > 450$  K) is the prerequisite for spintronic application. Therefore, in recent years, there have been constant efforts to break the fundamental limitations of the  $T_C$ . Park et al. grew the  $Mn_xGe_{1-x}$  ferromagnetic thin films on the GaAs substrate using the molecular beam epitaxy (MBE) technique [7]. The  $T_C$  value of these films increases linearly from 25 K to 116 K, with the Mn doping level increasing from 0.006 to 0.035. The relatively low solid solubility of Mn in the Ge matrix prevents the  $Mn_xGe_{1-x}$  alloy from obtaining a higher  $T_C$ . Many previous studies have shown that intermetallic compounds precipitate in  $Mn_xGe_{1-x}$  thin films with a high Mn doping level, such as  $Mn_5Ge_3$  ( $T_C \sim 296$  K) and  $Mn_{11}Ge_8$  ( $T_C \sim 270$  K) [8–10], for instance, with a typical Mn doping level higher than 0.05 [11]. Xiu et al. fabricated the pure-phase  $Mn_{0.05}Ge_{0.95}/Si$  quantum dots (QDs) [11,12]. Their  $T_C$  values, and the ferromagnetic temperature (FMT) manipulated by a static electric field were promoted to 400 and 100 K, respectively. The high- $T_C$  above 400 K achieved in MnGe QDs can probably be ascribed to at least two apparent advantages of the low dimensional nanostructure. First, the formation of metal precipitate phases is restrained in the low dimensional DFMS; this behavior increases the ratio of the doping Mn acting as the substitution atom and the localized Mn moment, rather than the interstitial one [13]. The other is that the generation of quantum-confined effects enhances the carrier localization and the exchange coupling between carriers and the localized Mn moment. Furthermore, the low dimensional DFMS with a  $T_C$  value above room temperature has also been demonstrated recently in other nanostructures, such as nanowires and nanotubes [14,15]. Although these achievements were accessed for the commercial application of the DFMSs, the current controllable FMT is still too low and should further improve at room temperature [16]. However, the systematically manipulating mechanisms of many common factors, such as Mn doping level, residual stress, and post-annealing, etc., on the ferromagnetism and the  $T_C$  value of the low dimensional MnGe DFMS are still absent. Additionally, almost all previously reported MnGe QDs, which are fabricated using the refined MBE technique, are usually deemed to have a relatively high cost and complicated processing method, and are not readily compatible with the so-called self-aligned silicide process [17].

Ion beam sputtering deposition (IBSD) is crucial for preparing high-quality thin films, demonstrating that high-quality epitaxial thin films and low dimensional nanomaterials could actualize through IBSD [17–21]. More importantly, the stress and relaxation in these lattice-mismatched nanostructures can be well-tuned by IBSD [22]. In this article, the IBSD technology used to grow the  $Mn_xGe_{1-x}$  QDs, and the growth mechanism and Mn-doping-level dependent ferromagnetic evolution of these DFMS QDs is addressed well.

## 2. Experimental Section

Ge-Mn composite target can be manufactured by pasting a certain amount of high purity Mn slices, each with a size of 5 mm  $\times$  5 mm  $\times$  0.5 mm, on a single crystal Ge target (99.999% purity, size of 70 mm  $\times$  70 mm). Figure 1 shows the several patterns of Mn slices distributed on a Ge target to increase the Mn doping level gradually in MnGe QDs. These slices are limited to a circle with a radius of  $\sim 3.53$  cm that corresponds to the largest bombardment area of the  $Ar^+$  ion beam.

The samples were grown on n-Si (001) substrate by using ion beam co-sputtering techniques. The Kaufman-type ion source (caliber: 30 mm) was used to generate an  $Ar^+$  ion beam [23]. The background vacuum and depositing Ar-gas pressure were  $2.3 \times 10^{-6}$  Torr and  $2.7 \times 10^{-4}$  Torr, respectively. The Si substrate was cleaned, first by using a modified Shiraki procedure [24]; then, the substrate was rinsed with 2.5% hydrofluoric acid (HF) to remove the natural oxide layer on the surface to obtain a hydrogen passivation surface. Finally, the substrate is dried with high-purity nitrogen and placed in a vacuum chamber.

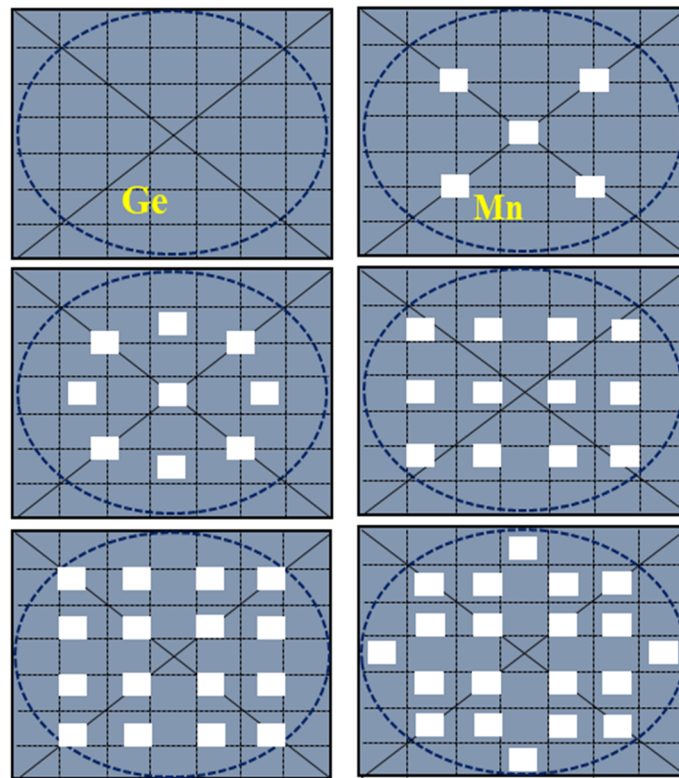


**Figure 1.** The patterns of Mn slices distributed on Ge target with an increase in Mn-slice number.

A 50 nm thick Si buffer layer was deposited at 750 °C before growing the  $\text{Mn}_x\text{Ge}_{1-x}$  QDs layer. The current settings for sputtering Si and Ge-Mn composite targets were 10 and 7 mA. As a result, the deposition rates of the Si buffer layer and the  $\text{Mn}_x\text{Ge}_{1-x}$  QDs layer, monitored by a quartz crystal oscillator, were 0.022 and 0.011 nm/s, respectively. The growth temperature of the  $\text{Mn}_x\text{Ge}_{1-x}$  QDs layer was set to 700 °C for all samples with different Mn concentrations, and the layer was deposited with a nominal thickness of about 3 nm. Immediately after depositing the  $\text{Mn}_x\text{Ge}_{1-x}$  layer, the samples were cooled to room temperature. Rapid thermal processing is used for post-annealing in a pure  $\text{N}_2$  environment at a temperature of 465 °C for 20 min.

The components of the sample surface were determined by using an energy dispersive X-ray spectrometer (EDX) equipped with a scanning electron microscopy (SEM) system. The surface morphologies of samples were measured ex situ by an atomic force microscope (AFM) in tapping mode. Raman scattering spectra were conducted with excitation wavelengths of 514.5 nm in the back-scattering geometry at room temperature. X-ray photoelectron spectroscopy analyses were carried out using a Thermo Scientific K-Alpha XPS system with a monochromatic Al  $K\alpha$  X-ray source. Magnetic measurements were performed in the Physical Property Measurement System (PPMS-9). The applied external magnetic field is parallel to the surface of the sample. The diamagnetic contribution from the substrate has been subtracted.

### 3. Results and Discussion

The composite Ge-Mn target can be manufactured by pasting a certain amount of high purity Mn slices onto a single crystal Ge target and the Mn doping level  $x$  in the  $\text{Mn}_x\text{Ge}_{1-x}$  QDs, as a function of the Mn slice number on the Ge target, can be construed. With the Mn-slice number increasing from 5 to 20, the actual Mn doping levels of 0.032, 0.046, 0.058, 0.068, and 0.075 can be determined by the X-ray energy spectrum, respectively, as shown in Figure 2a. Mn content in the MnGe QDs does not increase linearly with the Mn-slice number, but can be fitted well by an exponential function in Figure 2b. This dependence

starts to diverge from the nominal values based on the area ratio of all Mn-slices to Ge-target when the Mn-slice number is more than five. The main reason for this deviation is that the maximum coverage area of ion beam sputtering is a circular area with a radius of 3.5 cm. Since the sputtering area is not easy to control precisely, the actual sputtering area will be smaller than the theoretical area of the target.

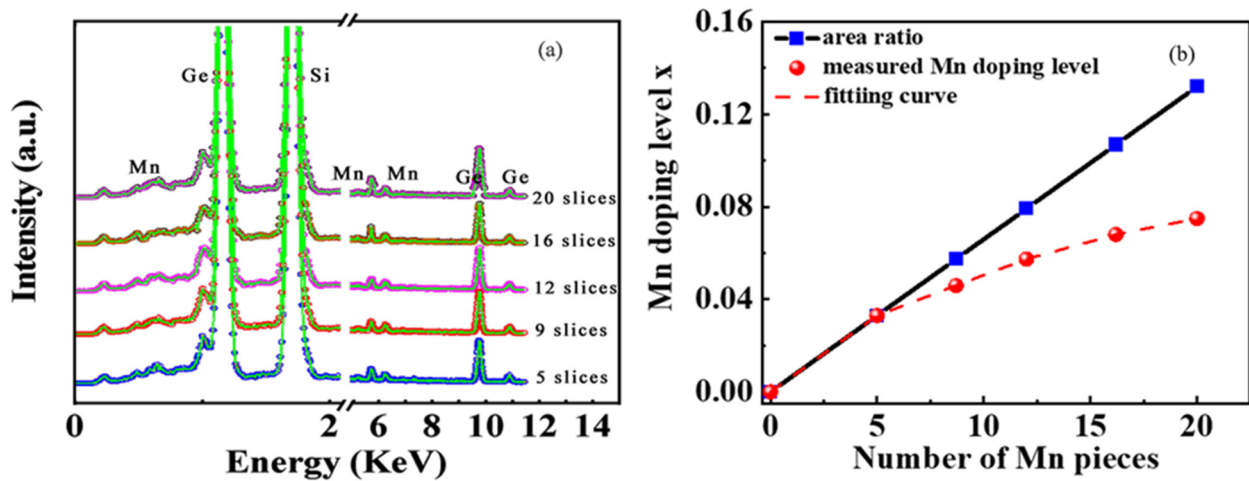


**Figure 2.** (a) The X-ray energy spectrum of the samples with an increase in Mn-slice number. (b) The Mn-slice number dependence of the Mn content  $x$  in the  $Mn_xGe_{1-x}$  film grown by ion beam co-sputtering.

The epitaxial growth mechanism of MnGe/Si QDs is close to that of Ge/Si QDs [11,12,16], and is based on the stress relaxation process originating from the lattice mismatch between Si and Ge. In the process, these QDs can be formed on the Si buffer layer by self-assembly via the Stranski–Krastanov (SK) growth mode, proving that IBSD is also an epitaxial growth technology [18]. Therefore, the growth of Ge/Si QDs by IBSD has been studied in detail [20,22,25]. In our work, MnGe/Si QDs with different Mn doping levels are prepared by IBSD. Figure 3 shows self-assembled MnGe QDs randomly distributed on Si substrate. The density of MnGe QDs decreases from  $1.4 \times 10^{10} \text{ cm}^{-2}$  to  $6.1 \times 10^9 \text{ cm}^{-2}$ , and the MnGe QDs size increases with the Mn content. These evolutions agreed with that of their counterparts grown by MBE [10]. Furthermore, similar density-decrease and size-increase behaviors found in the pure Ge QDs, which experienced the post-annealing process, were attributed to the diffusion of Ge adatom and the Ostwald ripening growth of Ge islands [26,27]. It suggested that the bonding amount of Mn-Ge during the initial stage of nucleation formation can enhance the diffusion of Ge adatom and favor ripening growth.

As shown in the statistical histograms in Figure 4, as the Mn doping increases from 0.046 to 0.075, both the average diameter and height of the  $Mn_{1-x}Ge_x$  QDs increase, from 75 nm to 100 nm and from 11 nm to 23 nm, respectively. The relatively drastic increase in the height of QDs probably can be profiled by comparing the average aspect ratio of these  $Mn_{1-x}Ge_x$  QDs. Yet, the number of small quantum dots decreased, while the large quantum dots appeared and increased. These phenomena suggest that the evolution mechanism of  $Mn_{1-x}Ge_x$  QDs follows the Ostwald ripening process with increasing Mn doping level [28].

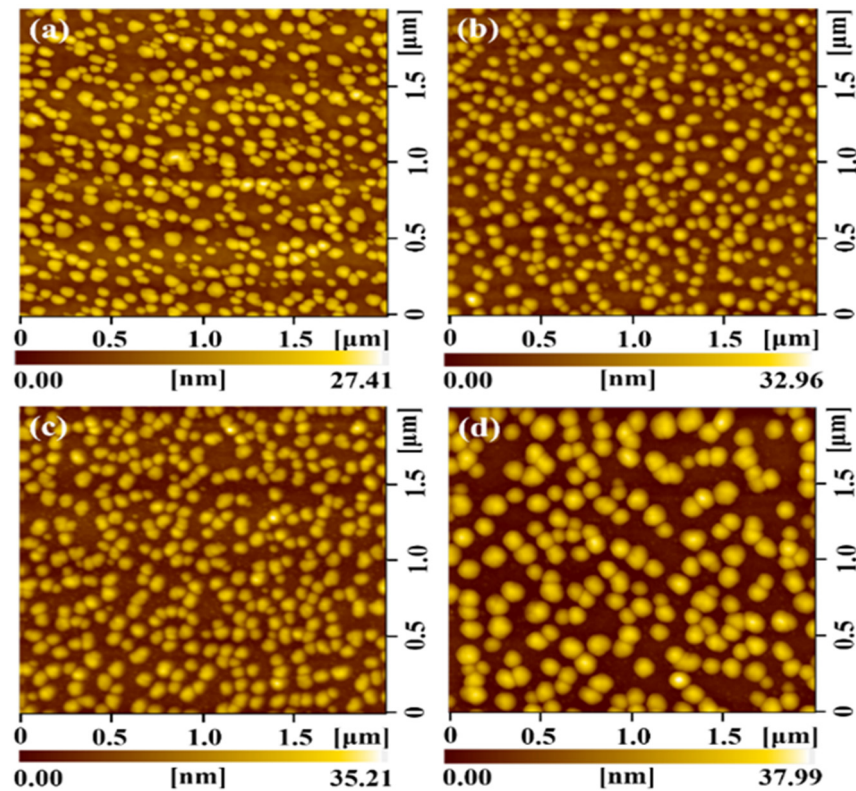


Figure 3. AFM surface morphology images of MnGe QD samples with Mn content of 4.6% (a), 5.8% (b), 6.8% (c) and 7.5% (d), respectively.

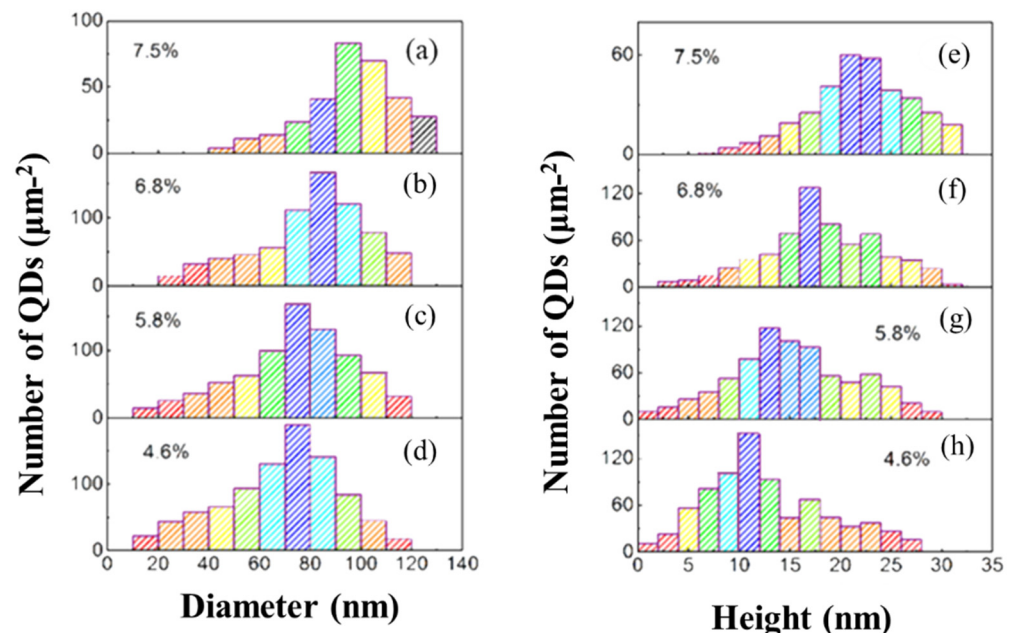
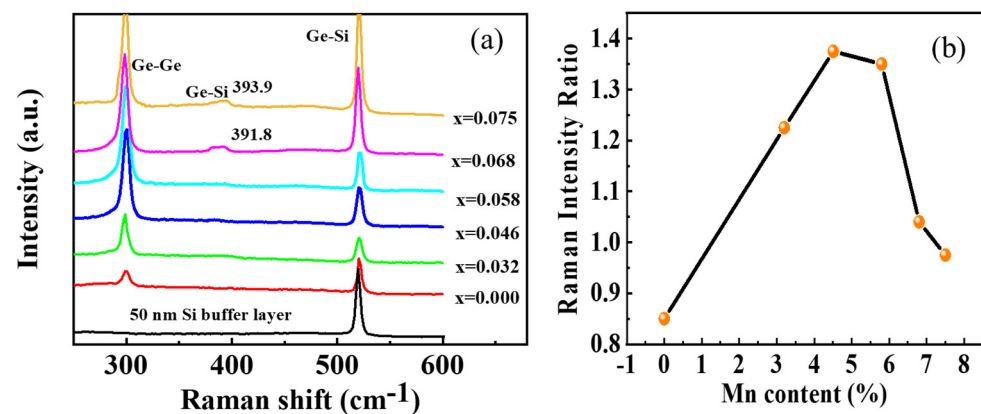


Figure 4. Statistic histograms for the diameter (a–d) and height (e–h) of the MnGe QDs at different Mn contents.

Usually, the evolution of QDs' size is accompanied by the variation in QDs' morphology [29]. According to the island shape's dependence on the contact-angle, the shape of Ge/Si QDs with a contact angle  $\theta$  less than  $7^\circ$  and larger than  $13^\circ$  can be classified as pre-pyramid and dome [30], respectively, and the rest of the Ge/Si QDs are pyramid or hut.

Increasing the Mn doping level from 0.046 to 0.075, the ratio of dome islands improved from 94% to 99%. It is proposed that the ferromagnetism of MnGe QDs originates primarily from the large dome-shaped MnGe QDs rather than the small hut-shaped ones [16]. Thus, the high ratio of dome islands realized in this work implies the stronger ferromagnetism of MnGe QDs.

As shown in Figure 5a, the sharp Raman peak at  $\sim 520\text{ cm}^{-1}$  originates from the Si-Si bond vibration of the Si buffer layer, indicating the high crystallinity of the Si buffer layer. The Raman shift of crystalline Ge peak at  $\sim 300\text{ cm}^{-1}$  does not change obviously with the variation in the Mn doping level, while the intensity ratio of Ge-Ge to Si-Si Raman peak varies significantly, as shown in Figure 5b. Actually, it first increases, then decreases with the increase in Mn doping level, and reaches its maximum of 1.37 in the  $\text{Mn}_{0.046}\text{Ge}_{0.954}$  QDs. It is interesting to note that the scattering intensity of Ge-Ge peak ( $I_{\text{Ge-Ge}}$ ) is stronger than that of Si-Si one ( $I_{\text{Si-Si}}$ ) in most of the  $\text{Mn}_x\text{Ge}_{1-x}$  QDs, except for those without doping and those with the maximal doping level ( $x = 0.075$ ). Generally, the relative intensity change in Raman peaks is proportional to the variation in a relative number of corresponding bonds in films [27]. In this experiment, the number of Ge-Ge bonds in the MnGe QDs samples decreases monotonically with the increase in Mn content, since the deposition time is the same for all QDs samples. However, the relative  $I_{\text{Ge-Ge}}$  value does not decrease correspondingly in the MnGe QDs samples, suggesting another factor dominates the variation in these Raman peaks.



**Figure 5.** (a) Raman spectra of the MnGe QDs samples with different Mn contents and the sample with only Si buffer layer. (b) Raman intensity ratio of Ge-Ge peak to Si-Si peak dependence of Mn concentration.

Surface-enhanced Raman spectroscopy (SERS) has been widely investigated by cladding Ag and Au films onto the surface of all kinds of samples, but little work is concerned with the transition metal coating. Recently, some organic films have demonstrated the SERS behaviors, including the Mn nanostructures [31]. This suggests that the abnormal Raman peak intensity observed in MnGe/Si QDs can be attributed to the surface-enhanced Raman scattering from Mn sites. Within this frame, the enhancement of surface plasmons in the MnGe layer is proposed to result in the increase in relative  $I_{\text{Ge-Ge}}$  values in the Mn doping level range from 0 to 0.046. However, the intensity ratio of  $I_{\text{Ge-Ge}}/I_{\text{Si-Si}}$  slightly decreases to 1.35 for the  $\text{Mn}_{0.058}\text{Ge}_{0.942}$  QDs, which is associated with the combined effect of the two factors. First, the enhanced Raman scattering of Ge-Ge bonds from surface plasmons can be weakened by the continuous reduction in the Ge-Ge bond amount as the Mn doping level reaches a relatively high level. Second, some Mn atoms can also diffuse into the Si buffer layer during the island growth and induce the Raman signal from Si-Si bonds to be enhanced by the surface plasmons simultaneously. The higher the Mn doping level, the more the Mn atoms diffuse into the buffer layer, and the stronger the enhanced intensity of Si-Si peak from surface plasmons. Both factors can lead to the continuous decrease in the  $I_{\text{Ge-Ge}}/I_{\text{Si-Si}}$  ratio. Once the Mn doping level is higher than 0.058, the Raman peak of Si-Ge

bonds appears at  $\sim 391\text{ cm}^{-1}$ , which indicates that the Si-Ge intermixing occurring in the islands results from the Ostwald ripening growth. Since the Ge content in Ge/Si islands can be calculated according to the Raman shifts of Ge-Ge and Si-Ge peaks [32,33], 90.9% and 89.1% in the  $\text{Mn}_{0.068}\text{Ge}_{0.932}$  and  $\text{Mn}_{0.075}\text{Ge}_{0.925}$  QDs, is determined by a similar method in which the Mn-doping related effects are neglected, only the Ge-Si intermixing is taken into account. Generally, the Ge-Si intermixing is inevitable in the Ge/Si QDs during the physical growth processes. This higher Ge composition in MnGe QDs is beneficial for increasing their Curie temperature [16]. Thus, it is worth noticing that the Ge chemical composition in the IBSD-grown Ge/Si QDs is higher than that in MBE-grown QDs [32,33], and a better ferromagnetism for MnGe QDs could be expected by using IBSD. For the  $\text{Mn}_{0.075}\text{Ge}_{0.925}$  QDs, the relative intensity  $I_{\text{Si-Si}}$  could further increase, even exceeding the  $I_{\text{Ge-Ge}}$  again. The depletion of Ge-Ge bonds via Ge-Si intermixing should also be considered at this Mn doping level.

To probe the role of Mn ions, we also characterized the chemical binding states of  $\text{Mn}_{0.068}\text{Ge}_{0.932}$  and  $\text{Mn}_{0.075}\text{Ge}_{0.925}$  QDs samples using the X-ray photoelectron spectroscopy (XPS) technique, as shown in Figure 6. In the former sample, the binding energies of Mn  $2p_{3/2}$  and Mn  $2p_{1/2}$  states are located at 641.4 eV and 653.3 eV, respectively, indicating the two valent states of the Mn ion [34–36]. The binding energies of the two states undergo a shift of  $-0.30\text{ eV}$  and  $0.50\text{ eV}$  in the latter sample, respectively. The blueshift of binding energy suggests that a higher valence state of Mn exists in the  $\text{Mn}_{0.075}\text{Ge}_{0.925}$  QDs sample [36]. Moreover, for the  $\text{Mn}_{0.068}\text{Ge}_{0.932}$  QDs, the peaks of Ge  $3d_{5/2}$  and Ge  $3d_{3/2}$  located at 29.32 eV and 29.82 eV can be ascribed to the zero valences of Ge, while those peaks located at 32.44 eV and 32.75 eV match with the +4 valence of Ge, respectively. With the doping level increasing from 0.068 to 0.075, the binding energy of zero-valent Ge shifts 0.15 eV and 0.30 eV, respectively, which implies the formation of the higher Ge valence states [37–39]. The coexistence of the higher valence states of both Mn and Ge in the  $\text{Mn}_{0.075}\text{Ge}_{0.925}$  QDs sample results from the formation of the second phase Mn-Ge structure [34].

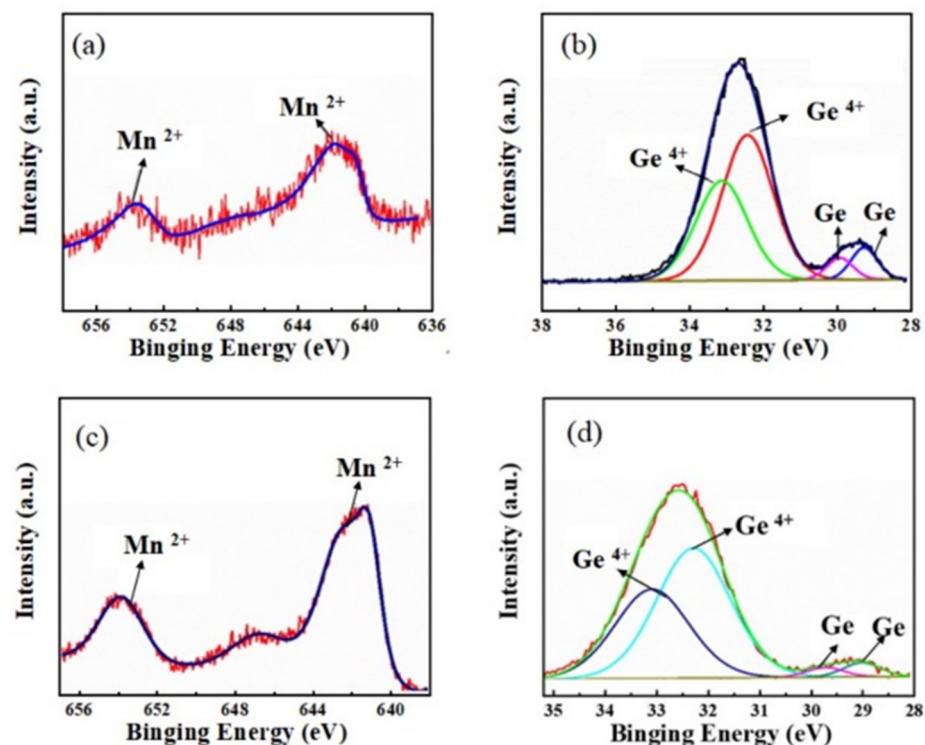
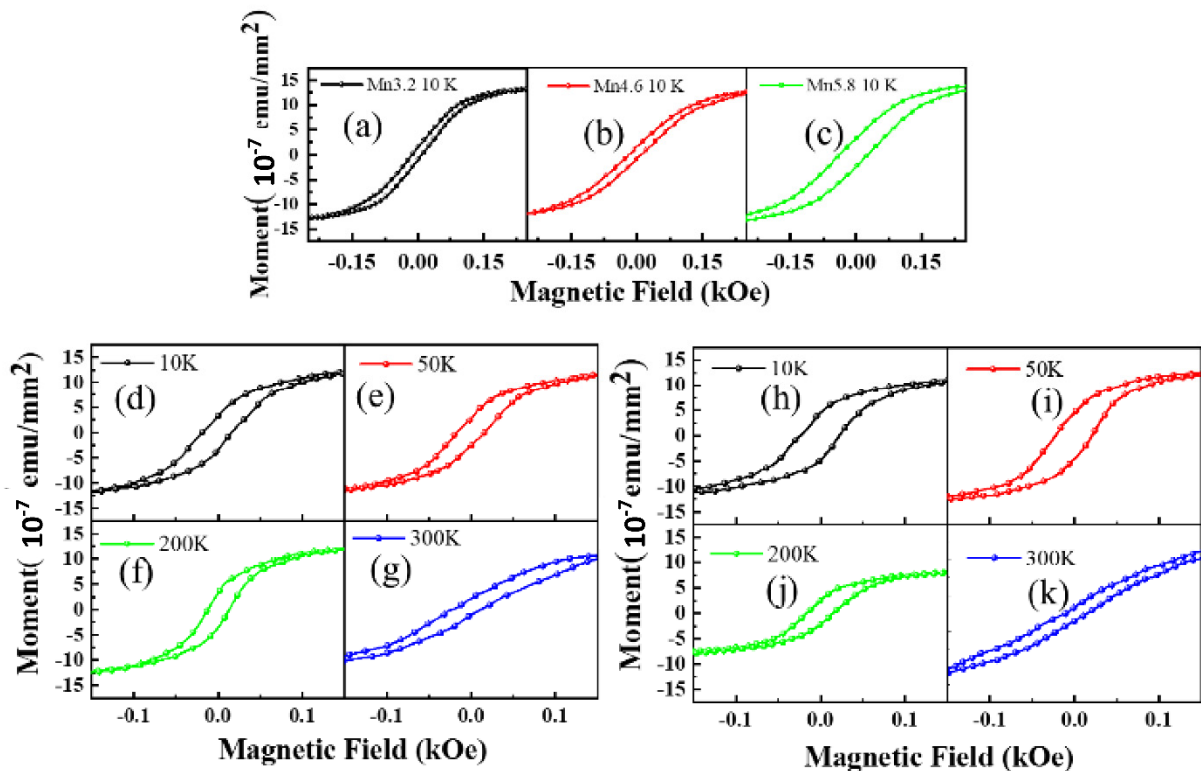


Figure 6. XPS spectra and their fitted lines for  $\text{Mn}_{0.068}\text{Ge}_{0.932}$  (a,b) and  $\text{Mn}_{0.075}\text{Ge}_{0.925}$  (c,d) QDs sample.

Therefore, the atomic structure of MnGe QDs has changed with the increase in the Mn doping level in the MnGe QDs samples. At a low doping level, the doping Mn atoms take the substitutional sites, and the crystal structure of QDs retains its diamond structure. However, at a high doping level, a new crystal structure accompanied by the possible formation of the intermetallic precipitate, such as  $\text{Mn}_5\text{Ge}_3$  with its lattice symmetry of  $P6_3/mcm$  [40], may also be produced and coexist with the diamond structure in the MnGe islands. Combined with the observation of AFM, Raman, and XPS, the composition and structure transition of QDs mainly occurs at the interface between the island bottom and the Si buffer, from the MnGe QDs, MnGeSi QDs, to MnGeSi QDs accompanied by a small quantity of precipitate, with an increase in the Mn doping level.

The magnetic properties of  $\text{Mn}_x\text{Ge}_{1-x}/\text{Si}$  QDs were characterized by the PPMS-9. The applied external magnetic field is parallel to the surface of the sample. Figure 7 shows the hysteresis loops of these QDs samples with different Mn doping levels, in which the diamagnetic contribution from the substrate has been subtracted. The remanence and coercive force of samples increases with the Mn doping concentration increasing from 0.032 to 0.058 (see Figure 7a), which indicates that the Curie temperature of  $\text{Mn}_x\text{Ge}_{1-x}$  QDs can be promoted effectively by simply increasing the Mn doping level. In addition, the hysteresis loops of  $\text{Mn}_{0.068}\text{Ge}_{0.932}$  and  $\text{Mn}_{0.075}\text{Ge}_{0.925}$  QDs were recorded at different temperatures, as shown in Figure 7d–k). At 300 K, the typical remanences of  $1.25 \times 10^{-7} \text{ emu}/\text{mm}^2$  and  $0.36 \times 10^{-7} \text{ emu}/\text{mm}^2$  can still be observed in  $\text{Mn}_{0.068}\text{Ge}_{0.932}$  and  $\text{Mn}_{0.075}\text{Ge}_{0.925}$  QDs, respectively, which suggests high  $T_C$  above room temperature.



**Figure 7.** The hysteresis loops of samples with different Mn dopant concentrations at different test temperatures. The hysteresis loops of  $\text{Mn}_{0.032}\text{Ge}_{0.968}$ ,  $\text{Mn}_{0.046}\text{Ge}_{0.954}$  and  $\text{Mn}_{0.058}\text{Ge}_{0.942}$  QDs samples at 10 K (a–c) and the hysteresis loops of  $\text{Mn}_{0.068}\text{Ge}_{0.932}$  (d–g) and  $\text{Mn}_{0.075}\text{Ge}_{0.925}$  QDs (h–k) samples at different temperatures from 10 K to 300 K, respectively. It is noted that the diamagnetic contributions from the substrates were subtracted.

Figure 8a shows the temperature dependence of magnetization for the samples with different Mn doping levels. Therein, the ferromagnetic signals in the  $\text{Mn}_{0.068}\text{Ge}_{0.932}$  QDs are most striking. Only one transition temperature (ferromagnetic phase) was observed in these

MnGe QDs with a low doping level (0.000–0.058). However, the magnetic moment below  $\sim 55$  K increases remarkably with further increasing the Mn doping level. Another transition temperature (paramagnetic phase) appears at  $\sim 55$  K in the  $\text{Mn}_{0.075}\text{Ge}_{0.925}$  QDs. Similar moment evolution of the  $\text{Mn}_{0.075}\text{Ge}_{0.925}$  QDs was observed in MBE-grown counterparts [11]. The appearance of a paramagnetic phase below 55 K can be attributed to Mn oxides or Mn/Ge/Si oxides on the island surface [3]. This suggests that the Mn oxides or Mn/Ge/Si oxides are easy to form at higher Mn doping levels due to the existence of excess Mn atoms.

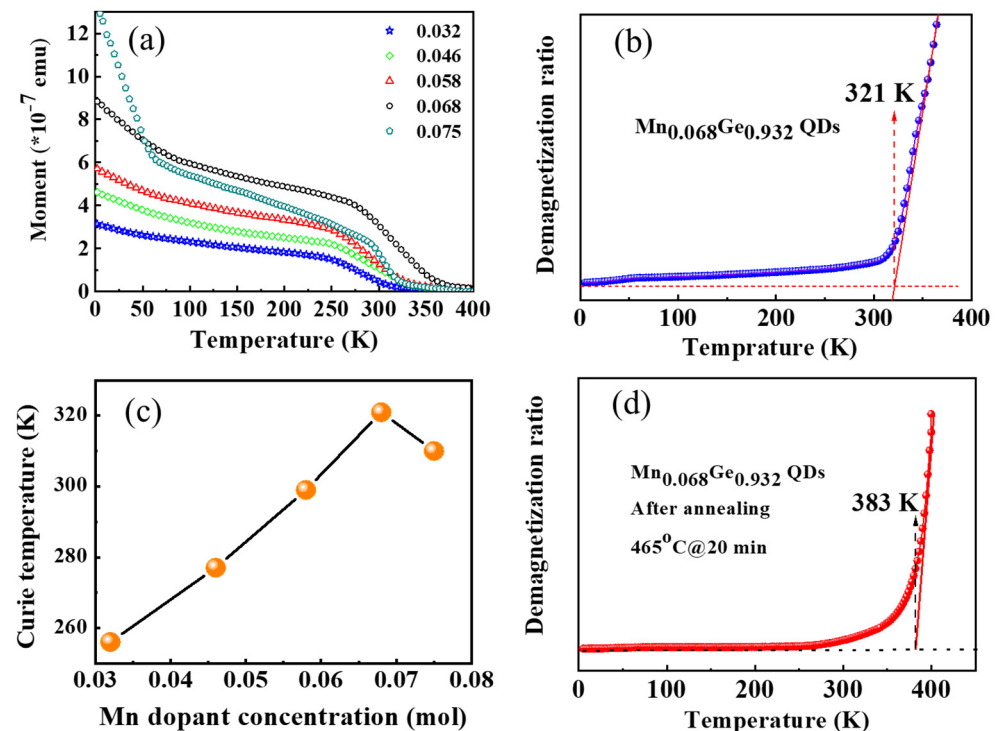


**Figure 8.** (a) Temperature dependence of magnetization for the samples with different Mn dopant concentrations. The testing temperature increased from 3 K to 400 K. An external magnetic field of 200 Oe is applied parallel to the sample surface. (b) The demagnetization ratio as a function of temperature for  $\text{Mn}_{0.068}\text{Ge}_{0.932}$  QDs sample. (c) Curie temperature dependence of Mn dopant concentration. (d) The demagnetization ratio as a function of temperature for  $\text{Mn}_{0.068}\text{Ge}_{0.932}$  QDs sample after annealing.

The  $T_C$  values of these MnGe QDs can be determined generally by fitting the temperature-dependent demagnetization ratio with the Curie–Weiss equation [3,11,41]. Results indicate that the maximal  $T_C$  value of 321 K is obtained in  $\text{Mn}_{0.068}\text{Ge}_{0.932}$  QDs, as shown in Figure 8b,c, respectively. The Curie temperature of the IBCS-grown samples does not increase monotonically with the increase in Mn doping levels, but decreases when Mn content is increased to 0.075. Hole-mediated effects generally dominate the ferromagnetism of the Mn-doped Ge alloy materials [3,11,14,42–44]. The localized Mn magnetic moments can be aligned to one direction by p–d exchange coupling between Mn ions and holes. Due to the stronger quantum confinement effect, the higher hole concentration confined in MnGe QDs can enhance the exchange coupling interaction and lead to the increase in the Curie temperature [6,45,46]. The exchange coupling interaction is enhanced with the increase in the Mn doping level until the formation of intermetallic precipitate at a relatively high Mn doping level. The formation of  $\text{Mn}_5\text{Ge}_{3-y}\text{Si}_y$  precipitates in  $\text{Mn}_{0.075}\text{Ge}_{0.925}$  QDs sample has been well confirmed by XPS spectra. The Curie temperature of  $\text{Mn}_5\text{Ge}_{3-y}\text{Si}_y$  precipitate is definite, such as  $\text{Mn}_5\text{Ge}_3$  and  $\text{Mn}_5\text{GeSi}_2$  precipitate is 296 K and 225 K, respectively [15,47–49], which are lower than that of  $\text{Mn}_{0.068}\text{Ge}_{0.932}$  QDs. Therefore, the

existence of intermetallic precipitate depresses the ferromagnetic order in QDs and the further increase in the Curie temperature in the  $\text{Mn}_{0.075}\text{Ge}_{0.925}$  QDs sample.

Both a residual strain and a higher Ge composition in QDs can benefit the formations of ferromagnetic phase Mn-doped Ge QDs. As shown in Figure 5, the Raman peak of the Si-Ge bond does not present until the Mn doping level is higher than 0.058, which suggests that Ge composition in the IBCS-grown MnGe QDs is higher than that in MBE-grown QDs. Furthermore, it is proposed that a strong residual strain is still left in undoped Ge QDs fabricated by using the IBCS [22,50]. These results suggest that IBCS is beneficial to forming Mn-doped Ge QDs with a good ferromagnetic phase. Although the maximal Curie temperature of MnGe QDs in this work does not reach 400 K, which is the highest Curie temperature of MnGe QDs reported in the literature [42], the overall  $T_C$  values of the IBCS-grown MnGe QDs are superior to most of those with similar Mn doping levels grown by MBE [3,15]. To further enhance the ferromagnetism of MnGe QDs grown by IBCS, rapid thermal annealing for the  $\text{Mn}_{0.068}\text{Ge}_{0.932}$  QDs samples were subjected to rapid thermal annealing at 465 °C for 20 min in a pure  $\text{N}_2$  environment. As shown in Figure 8d, the  $T_C$  value of this sample increased from 321 K to 383 K after the post-annealing treatment; this suggested that a part of the defects in MnGe QDs were repaired during the post-annealing process; the FM order is well enhanced, correspondingly. However, more work on annealing is needed to reveal the ferromagnetic modulation of the MnGe QDs.

#### 4. Conclusions

The Mn doping level dependent microstructure and ferromagnetism of  $\text{Mn}_x\text{Ge}_{1-x}/\text{Si}$  QDs were systematically investigated using ion beam co-sputtering technology. The ripening growth of  $\text{Mn}_x\text{Ge}_{1-x}$  QDs, driven by self-assembly via the Stranski–Krastanov (SK) growth mode, was identified to result in a size increase and a density decrease in the  $\text{Mn}_x\text{Ge}_{1-x}$  island with an increase in the Mn doping level. The distribution behavior of Mn atoms in QDs and Si buffer layers are well elucidated, based on the observation of the surface-enhanced Raman scattering effects. An optimal Mn doping level of 0.068 created the highest Curie temperature of MnGe QDs obtained in the investigated doping range; further increasing the Mn doping level to 0.075 decreased the Curie temperature, probably due to the formation of intermetallic precipitates in MnGe QDs. The steady enhancement of ferromagnetism has been demonstrated in the post-annealed  $\text{Mn}_{0.068}\text{Ge}_{0.932}$  QDs sample by increasing the Curie temperature from 321 K to 383 K. Our results indicate that ion beam co-sputtering can be an effective alternative method for fabricating ferromagnetic nanomaterials. The highly ferromagnetic performance of  $\text{Mn}_x\text{Ge}_{1-x}$  QDs confirmed in this work is conducive to accelerating the realization of the excellent engineering of full Si-based spintronic and micro-electronic integration.

**Author Contributions:** J.Y. (Jing Yang), C.L. (Chen Li), C.L. (Chunjiang Lu), X.H. and L.Z. performed formal analysis; S.Y. and H.C. performed the investigation; F.Q. provided resources; R.W., J.Y. (Jie Yang) and C.W. supervised the whole study; X.D. and S.Y. drafted the manuscript. All authors have read and agreed to the published version of the manuscript.

**Funding:** This work was financially supported by the National Natural Science Foundation of China [No. 12164051, 11704330, 62064013]; Joint Foundation of Yunnan Provincial Science and Technology Department and Double-First-class Construction of Yunnan University [No. 2019FY003016], Young Top Talent Project of Yunnan Province [No. YNWR-QNBj-2018-229], and the Application Basic Research Project [No. 2019FB130] of Yunnan Province.

**Data Availability Statement:** The data presented in this study are available in this article.

**Acknowledgments:** X. Duan thanks Advanced Analysis and Measurement Center of Yunnan University for the sample characterization service.

**Conflicts of Interest:** The authors declare no conflict of interest.

## References

1. Awschalom, D.D.; Flatte, M.E. Challenges for semiconductor spintronics. *Nat. Phys.* **2007**, *3*, 153–159. [[CrossRef](#)]
2. Dietl, T. A ten-year perspective on dilute magnetic semiconductors and oxides. *Nat. Mater.* **2010**, *9*, 965–974. [[CrossRef](#)] [[PubMed](#)]
3. Wang, L.; Liu, T.; Hu, X.; Wang, S.; Zhong, Z.; Jia, Q.; Jiang, Z. Carrier effects on ferromagnetism of  $\text{Mn}_x\text{Ge}_{1-x}$  quantum dots. *Appl. Phys. Lett.* **2017**, *111*, 072103. [[CrossRef](#)]
4. Dietl, T.; Ohno, H. Dilute ferromagnetic semiconductors: Physics and spintronic structures. *Rev. Mod. Phys.* **2014**, *86*, 187–251. [[CrossRef](#)]
5. Cai, B.; Chen, X.; Xie, M.; Zhang, S.; Liu, X.; Yang, J.; Zhou, W.; Guo, S.; Zeng, H. A class of Pb-free double perovskite halide semiconductors with intrinsic ferromagnetism, large spin splitting and high Curie temperature. *Mater. Horiz.* **2018**, *5*, 961–968. [[CrossRef](#)]
6. Park, Y.D.; Hanbicki, A.T.; Erwin, S.C.; Hellberg, C.S.; Sullivan, J.M.; Mattson, J.E.; Ambrose, T.F.; Wilson, A.; Spanos, G.; Jonker, B.T. A group-IV ferromagnetic semiconductor:  $\text{Mn}_x\text{Ge}_{1-x}$ . *Science* **2002**, *295*, 651–654. [[CrossRef](#)]
7. Wang, Y.; Zou, J.; Zhao, Z.; Han, X.; Zhou, X.; Wang, K.L. Direct structural evidences of  $\text{Mn}_{11}\text{Ge}_8$  and  $\text{Mn}_5\text{Ge}_2$  clusters in  $\text{Ge}_{0.96}\text{Mn}_{0.04}$  thin films. *Appl. Phys. Lett.* **2008**, *92*, 101913. [[CrossRef](#)]
8. Park, Y.D.; Wilson, A.; Hanbicki, A.T.; Mattson, J.E.; Ambrose, T.; Spanos, G.; Jonker, B.T. Magnetoresistance of Mn:Ge ferromagnetic nanoclusters in a diluted magnetic semiconductor matrix. *Appl. Phys. Lett.* **2001**, *78*, 2739–2741. [[CrossRef](#)]
9. Wang, Y.; Zou, J.; Zhao, Z.; Han, X.; Zhou, X.; Wang, K.L. Mn behavior in  $\text{Ge}_{0.96}\text{Mn}_{0.04}$  magnetic thin films grown on Si. *J. Appl. Phys.* **2008**, *103*, 066104. [[CrossRef](#)]
10. Kassim, J.; Nolph, C.; Jamet, M.; Reinke, P.; Floro, J.  $\text{Ge}_{1-x}\text{Mn}_x$  heteroepitaxial quantum dots: Growth, morphology, and magnetism. *J. Appl. Phys.* **2013**, *113*, 073910. [[CrossRef](#)]
11. Xiu, F.; Wang, Y.; Kim, J.; Hong, A.; Tang, J.; Jacob, A.P.; Zou, J.; Wang, K.L. Electric-field-controlled ferromagnetism in high-Curie-temperature  $\text{Mn}_{0.05}\text{Ge}_{0.95}$  quantum dots. *Nat. Mater.* **2010**, *9*, 337–344. [[CrossRef](#)] [[PubMed](#)]
12. Shaughnessy, M.; Fong, C.Y.; Snow, R.; Yang, L.H.; Chen, X.S.; Jiang, Z.M. Structural and magnetic properties of single dopants of Mn and Fe for Si-based spintronic materials. *Phys. Rev. B* **2010**, *82*, 035202. [[CrossRef](#)]
13. Kazakova, O.; Kulkarni, J.S.; Holmes, J.D.; Demokritov, S.O. Room-temperature ferromagnetism in  $\text{Ge}_{1-x}\text{Mn}_x$  nanowires. *Phys. Rev. B* **2005**, *72*, 094415. [[CrossRef](#)]
14. Nie, T.; Tang, J.; Kou, X.; Gen, Y.; Lee, S.; Zhu, X.; He, Q.; Chang, L.T.; Murata, K.; Fan, Y.; et al. Enhancing electric-field control of ferromagnetism through nanoscale engineering of high-Tc  $\text{Mn}_x\text{Ge}_{1-x}$  nanomesh. *Nat. Commun.* **2016**, *7*, 12866. [[CrossRef](#)]
15. Wang, L.; Liu, T.; Jia, Q.; Zhang, Z.; Lin, D.; Chen, Y.; Fan, Y.; Zhong, Z.; Yang, X.; Zou, J.; et al. Research Update: Strain and composition effects on ferromagnetism of  $\text{Mn}_{0.05}\text{Ge}_{0.95}$  quantum dots. *APL Mater.* **2016**, *4*, 040701. [[CrossRef](#)]
16. Assaf, E.; Portavoce, A.; Houmada, K.; Bertoglio, M.; Bertaina, S. High Curie temperature  $\text{Mn}_5\text{Ge}_3$  thin films produced by non-diffusive reaction. *Appl. Phys. Lett.* **2017**, *110*, 072408. [[CrossRef](#)]
17. Sasaki, K.; Nabetani, Y.; Miyashita, H.; Hata, T. Heteroepitaxial growth of SiGe films and heavy B doping by ion-beam sputtering. *Thin Solid Films* **2000**, *369*, 171–174. [[CrossRef](#)]
18. Sasaki, K.; Nakata, K.; Hata, T. Epitaxial growth of SiGe thin films by ion-beam sputtering. *Appl. Surf. Sci.* **1997**, *113*, 43–47. [[CrossRef](#)]
19. Wang, C.; Ke, S.Y.; Yang, J.; Hu, W.D.; Qiu, F.; Wang, R.F.; Yang, Y. Electronic properties of single Ge/Si quantum dot grown by ion beam sputtering deposition. *Nanotechnology* **2015**, *26*, 105201. [[CrossRef](#)]
20. Yang, J.; Zhao, B.; Wang, C.; Qiu, F.; Wang, R.; Yang, Y. Improving the growth of Ge/Si islands by modulating the spacing between screen and accelerator grids in ion beam sputtering deposition system. *Appl. Surf. Sci.* **2016**, *386*, 303–308. [[CrossRef](#)]
21. Zhang, Z.; Wang, R.F.; Zhang, J.; Li, H.S.; Zhang, J.; Qiu, F.; Yang, J.; Wang, C.; Yang, Y. Direct growth of Ge quantum dots on a graphene/SiO<sub>2</sub>/Si structure using ion beam sputtering deposition. *Nanotechnology* **2016**, *27*, 305601. [[CrossRef](#)] [[PubMed](#)]
22. Chung, H.-C.; Liu, C.-P.; Lai, Y.-L. Formation of coherent Ge shallow dome islands on Si(001) by ultra-high-vacuum ion beam sputter deposition. *Appl. Phys. A* **2008**, *91*, 267–271. [[CrossRef](#)]
23. Gnanarajan, S.; Savvides, N. Dual ion beam assisted magnetron deposition of biaxially textured YSZ and YBCO/YSZ thin films. *Surf. Coat. Tech.* **2016**, *305*, 116–122. [[CrossRef](#)]
24. Ishizaka, A.; Shiraki, Y. Low-Temperature Surface Cleaning of Silicon and Its Application to Silicon Mbe. *J. Electrochem. Soc.* **1986**, *133*, 666–671. [[CrossRef](#)]
25. Ke, S.; Ye, S.; Yang, J.; Wang, Z.; Wang, C.; Yang, Y. Morphological evolution of self-assembled SiGe islands based on a mixed-phase pre-SiGe island layer grown by ion beam sputtering deposition. *Appl. Surf. Sci.* **2015**, *328*, 387–394. [[CrossRef](#)]
26. Shu, Q.; Wang, R.; Yang, J.; Zhang, M.; Zeng, T.; Sun, T.; Wang, C.; Yang, Y. Microstructure and optical response optimization of Ge/Si quantum dots transformed from the sputtering-grown Ge thin film by manipulating the thermal annealing. *Nanotechnology* **2018**, *29*, 095601. [[CrossRef](#)]
27. Singha, R.K.; Das, S.; Majumdar, S.; Das, K.; Dhar, A.; Ray, S.K. Evolution of strain and composition of Ge islands on Si (001) grown by molecular beam epitaxy during postgrowth annealing. *J. Appl. Phys.* **2008**, *103*, 114301. [[CrossRef](#)]
28. Ferri, F.A. Low-temperature metal-induced crystallization of Mn-containing amorphous Ge thin films. *J. Non-Cryst. Solids* **2012**, *358*, 58–60. [[CrossRef](#)]

29. Montalenti, F.; Raiteri, P.; Migas, D.B.; von Kanel, H.; Rastelli, A.; Manzano, C.; Costantini, G.; Denker, U.; Schmidt, O.G.; Kern, K.; et al. Atomic-scale pathway of the pyramid-to-dome transition during ge growth on Si(001). *Phys. Rev. Lett.* **2004**, *93*, 216102. [[CrossRef](#)]
30. Huang, C.J.; Zuo, Y.H.; Li, D.Z.; Cheng, B.W.; Luo, L.P.; Yu, J.Z.; Wang, Q.M. Shape evolution of Ge/Si(001) islands induced by strain-driven alloying. *Appl. Phys. Lett.* **2001**, *78*, 3881–3883. [[CrossRef](#)]
31. Savaloni, H.; Goli-Haghighi, S.; Babaei, R. Application of Mn-Cu Helical Star-Shaped (Pine-Tree-Like) Sculpted Thin Films with Different Symmetries Using Surface-Enhanced Raman Spectroscopy (SERS). *Appl. Spectrosc.* **2019**, *73*, 879–892. [[CrossRef](#)] [[PubMed](#)]
32. Lin, J.H.; Yang, H.B.; Qin, J.; Zhang, B.; Fan, Y.L.; Yang, X.J.; Jiang, Z.M. Strain analysis of Ge/Si(001) islands after initial Si capping by Raman spectroscopy. *J. Appl. Phys.* **2007**, *101*, 083528. [[CrossRef](#)]
33. Alonso, M.I.; de la Calle, M.; Ossó, J.O.; Garriga, M.; Goñi, A.R. Strain and composition profiles of self-assembled Ge/Si(001) islands. *J. Appl. Phys.* **2005**, *98*, 033530. [[CrossRef](#)]
34. Qiao, S.; Hou, D.; Wei, Y.; Gao, W.; Hu, Y.; Zhen, C.; Tang, G. Ferromagnetism in  $Mn_xGe_{1-x}$  films prepared by magnetron sputtering. *J. Magn. Magn. Mater.* **2009**, *321*, 2446–2450. [[CrossRef](#)]
35. Kim, S.-K.; Cho, Y.C.; Jeong, S.-Y.; Cho, C.-R.; Park, S.E.; Lee, J.H.; Kim, J.-P.; Kim, Y.C.; Choi, H.W. High-temperature ferromagnetism in amorphous semiconductor  $Ge_3Mn$  thin films. *Appl. Phys. Lett.* **2007**, *90*, 192505. [[CrossRef](#)]
36. Qiao, S.; Hou, D.; Wei, Y.; Zhang, Q.; Zhen, C. Structure, magnetic and transport properties of  $Mn_xGe_{1-x}$  films. *Physica B* **2008**, *403*, 3916–3920. [[CrossRef](#)]
37. Sato, S.; Nozaki, S.; Morisaki, H. Photo-oxidation of germanium nanostructures deposited by the cluster-beam evaporation technique. *J. Appl. Phys.* **1997**, *81*, 1518–1521. [[CrossRef](#)]
38. Craciun, V.; Boyd, I.W.; Reader, A.H.; Vandenhoudt, D.E.W. Low temperature synthesis of Ge nanocrystals in  $SiO_2$ . *Appl. Phys. Lett.* **1994**, *65*, 3233–3235. [[CrossRef](#)]
39. Craciun, V.; Boyd, I.W.; Craciun, D.; Andreazza, P.; Perriere, J. Vacuum ultraviolet annealing of hydroxyapatite films grown by pulsed laser deposition. *J. Appl. Phys.* **1999**, *85*, 8410–8414. [[CrossRef](#)]
40. Shinya, H.; Fukushima, T.; Masago, A.; Sato, K.; Katayama-Yoshida, H. First-principles calculations on the origin of ferromagnetism in transition-metal doped Ge. *Phys. Rev. B* **2017**, *96*, 104415. [[CrossRef](#)]
41. Thaljaoui, R.; Pekała, K.; Pekała, M.; Boujelben, W.; Szydłowska, J.; Fagnard, J.F.; Vanderbemden, P.; Cheikhrouhou, A. Magnetic susceptibility and electron magnetic resonance study of monovalent potassium doped manganites  $Pr_{0.6}Sr_{0.4-x}K_xMnO_3$ . *J. Alloys Compd.* **2013**, *580*, 137–142. [[CrossRef](#)]
42. Nie, T.; Kou, X.; Tang, J.; Fan, Y.; Lee, S.; He, Q.; Chang, L.T.; Murata, K.; Gen, Y.; Wang, K.L. Nanoengineering of an Si/MnGe quantum dot superlattice for high Curie-temperature ferromagnetism. *Nanoscale* **2017**, *9*, 3086–3094. [[CrossRef](#)] [[PubMed](#)]
43. Xiu, F.; Wang, Y.; Wong, K.; Zhou, Y.; Kou, X.; Zou, J.; Wang, K.L. MnGe magnetic nanocolumns and nanowells. *Nanotechnology* **2010**, *21*, 255602. [[CrossRef](#)] [[PubMed](#)]
44. Xiu, F.; Ovchinnikov, I.V.; Upadhyaya, P.; Wong, K.; Kou, X.; Zhou, Y.; Wang, K.L. Voltage-controlled ferromagnetic order in MnGe quantum dots. *Nanotechnology* **2010**, *21*, 375606. [[CrossRef](#)]
45. Chiba, D.; Sawicki, M.; Nishitani, Y.; Nakatani, Y.; Matsukura, F.; Ohno, H. Magnetization vector manipulation by electric fields. *Nature* **2008**, *455*, 515–518. [[CrossRef](#)]
46. Dietl, T.; Ohno, H.; Matsukura, F.; Cibert, J.; Ferrand, D. Zener model description of ferromagnetism in zinc-blende magnetic semiconductors. *Science* **2000**, *287*, 1019–1022. [[CrossRef](#)]
47. De Padova, P.; Olivieri, B.; Mariot, J.M.; Favre, L.; Berbezier, I.; Quaresima, C.; Paci, B.; Generosi, A.; Rossi Albertini, V.; Cricenti, A.; et al. Ferromagnetic Mn-doped  $Si_{0.3}Ge_{0.7}$  nanodots self-assembled on Si(100). *J. Phys. Condens. Matter* **2012**, *24*, 142203. [[CrossRef](#)]
48. Arras, E.; Lançon, F.; Slipukhina, I.; Prestat, É.; Rovezzi, M.; Tardif, S.; Titov, A.; Bayle-Guillemaud, P.; d’Acapito, F.; Barski, A.; et al. Interface-driven phase separation in multifunctional materials: The case of the ferromagnetic semiconductor GeMn. *Phys. Rev. B* **2012**, *85*, 115204. [[CrossRef](#)]
49. Ferri, F.A.; Pereira-da-Silva, M.A.; Zanatta, A.R.; Varella, A.L.S.; de Oliveira, A.J.A. Effect of Mn concentration and atomic structure on the magnetic properties of Ge thin films. *J. Appl. Phys.* **2010**, *108*, 113922. [[CrossRef](#)]
50. Yang, J.; Jin, Y.; Wang, C.; Li, L.; Tao, D.; Yang, Y. Evolution of self-assembled Ge/Si island grown by ion beam sputtering deposition. *Appl. Surf. Sci.* **2012**, *258*, 3637–3642. [[CrossRef](#)]